



RESEARCH ARTICLE

10.1029/2021JD034575

Key Points:

- Meso-scale patterns of trade-wind clouds are identified with a neural network and characterized based on observations
- The four analyzed patterns distinguish themselves by stratiform cloudiness and less by cloudiness at the lifting condensation level
- Two patterns are imprinted by tropical, respectively extra-tropical intrusions

Supporting Information:

Supporting Information may be found in the online version of this article.

Correspondence to:

H. Schulz,
hauke.schulz@mpimet.mpg.de

Citation:

Schulz, H., Eastman, R., & Stevens, B. (2021). Characterization and evolution of organized shallow convection in the downstream North Atlantic trades. *Journal of Geophysical Research: Atmospheres*, 126, e2021JD034575. <https://doi.org/10.1029/2021JD034575>

Received 13 JAN 2021

Accepted 28 JUL 2021

Characterization and Evolution of Organized Shallow Convection in the Downstream North Atlantic Trades

Hauke Schulz¹ , Ryan Eastman² , and Bjorn Stevens¹

¹Max Planck Institute for Meteorology, Hamburg, Germany, ²University of Washington, Seattle, WA, USA

Abstract Four previously identified patterns of meso-scale cloud organization in the trades — called *Sugar*, *Gravel*, *Flowers*, and *Fish* — are studied using long-term records of ground-based measurements, satellite observations and reanalyses. A deep neural network trained to detect these patterns is applied to satellite imagery to identify periods during which a particular pattern is observed over the Barbados Cloud Observatory. Surface-based remote sensing at the observatory is composited and shows that the patterns can be distinguished by differences in cloud geometry. Variations in total cloudiness among the patterns are dominated by variations in cloud-top cloudiness. Cloud amount near cloud base varies little. Each pattern is associated with a distinct atmospheric environment whose characteristics are traced back to origins that are not solely within the trades. *Sugar* air-masses are characterized by weak winds and of tropical origin. *Fish* are driven by convergence lines originating from synoptical disturbances. *Gravel* and *Flowers* are most native to the trades, but distinguish themselves with slightly stronger winds and stronger subsidence in the first case and greater stability in the latter. The patterns with the higher cloud amounts and more negative cloud-radiative effects, *Flowers* and *Fish*, are selected by conditions expected to occur less frequently with greenhouse warming.

1. Introduction

The organization of deep convection has long been recognized to influence the global distribution of moisture and, as a consequence, the climate. Shallow convection, as is common in the trades, is usually not thought of as being organized. Rather, in the mind's eye of many researchers, trade-wind clouds are randomly distributed, have little vertical development and have generally been assumed to play little role in the climate system. Over the past twenty years however, the out-sized role of maritime shallow clouds on Earth's radiation budget — and discrepancies in how models predict their changes with warming (Bony & Dufresne, 2005) — have made a determination of processes controlling their coverage a central focus of climate science. During this period, observational studies such as RICO (Rauber et al., 2007) and the emergence of satellite imagery with spatial resolution on the hectometer scale began emphasizing how shallow clouds in the trades adopt different forms of organization, often in association with precipitation development and the formation of cold pools (Seifert & Heus, 2013; Seifert et al., 2015; Zuidema et al., 2012). More recently, several approaches to characterize these forms of organizations have been developed (Denby, 2020; Janssens et al., 2021; Stevens et al., 2020). Stevens et al. (2020) identified that most of the large-scale patterns of shallow convection can be categorized into four categories, which they called *Sugar*, *Gravel*, *Flowers*, and *Fish*. Although based solely on the subjective visual inspection of visible satellite imagery in the vicinity of the Barbados Cloud Observatory (BCO), these patterns have varied net cloud radiative effects and thus may influence Earth's climate sensitivity (Bony et al., 2020).

In contrast to Denby (2020) and Janssens et al. (2021) who retrieve a continuum of classes, the limitation to the few categories of Stevens et al. (2020) helps to break down natures' complexity into manageable pieces, arguably the building blocks of shallow convection in the downstream trades. Understanding what factors help select these patterns may help understand factors controlling cloudiness as a whole.

Motivated by the potential impact on climate sensitivity and the striking differences in the visual appearance of the four patterns identified by Stevens et al. (2020), we are interested in better understanding the basic features of these four patterns, and the factors that influence their emergence. Specifically:

- How do the four patterns differ in terms of the observed cloud geometry for example, cloud fraction, cloud size, and cloud base height?

© 2021. The Authors.

This is an open access article under the terms of the Creative Commons Attribution License, which permits use, distribution and reproduction in any medium, provided the original work is properly cited.

Table 1
Primary Data

Platform	Instrument	Variables	Location	Sampling
GOES-16	ABI	brightness temperature (channel 13)	10°N - 24°N; 61°W - 40°W	2 km; 30 min
AQUA	MODIS	- brightness temperature (ch. 31) - corrected reflectance (ch. 1,3,4)	10°S - 55°N; 100°W - 10°E	daily (daytime overpass)
ERA5	n/a	ω , div, T, u, v, SST	0°N - 60°N; 70°W - 10°E	0.25° × 0.25°; 3 h
BCO	- Ka-Band radar - Raman lidar - MRR - weather sensor - microwave radiometer - soundings	- reflectivity profile - mixing ratio profile (only Figure 2) - rain rate - surface p, T, RH, u, v - LWP, IWV - p, T, RH, u, v	13.16°N; 59.43°W	- 10 s; 30 m - 120 s; 60 m - 60 s - 10 s - 1 s
Grandley Adams Airport			13.07°N; 59.50°W	12–24 h

2. Are the different patterns associated with different large-scale environments?
3. To what extent are these large-scale differences reflective of different air mass origins?

To answer these questions we collocate the four cloud patterns of meso-scale organization as automatically detected in satellite measurements with observations made at the BCO. This contextualization of the high-resolution ground-based cloud measurements within the meso-scale patterning enables deeper insights about their characteristics than possible using satellite measurements alone.

The methods adopted and the data used are described in Section 2. A characterization of the cloud patterns, with a focus on the cloud-geometric properties and how they fit with our preconceptions as derived from the satellite images is given in Section 3. In Section 4 we analyze the meteorological conditions under which the patterns occur and the extent to which they can be distinguished. The effects of air-mass origin are analyzed with the aid of back-trajectories in Section 5. We conclude with Section 6.

2. Data and Methods

This study uses several data sources as shown in Table 1.

2.1. Pattern Detection of Shallow Convection

To detect the four patterns of shallow convection, we use the Keras RetinaNet (Gaiser et al., 2018). We trained this deep neural network (in the following just neural network), as described in Rasp et al. (2020) with only a difference in the input data's radiance. While we used the same 49,000 manually created labels that were performed based on 10 years of visible imagery captured by the Moderate Resolution Imaging Spectroradiometer (MODIS) instruments aboard the satellites AQUA and TERRA, here we use the simultaneously captured brightness temperatures.

To capture the inter-pattern variability at a fixed site, like the BCO, it needs to be assumed, that the patterns persist for at least the time it takes to advect over the site. In case of the patterns studied here, the characteristic length scale of a typical pattern can easily exceed 90 km, or about 3 h, for an advection speed of 8 m s^{-1} . However, 3 h is about the time between AQUA and TERRA overpasses, where we have noticed differences in the distribution of pattern types. Using infrared data allows us to overcome this issue by also retrieving useful classifications at night and increasing the number of classifications per day, even more so by applying the neural network to infrared satellite imagery taken by the Advanced Baseline Imager (ABI) aboard GOES-16. Although the training of a separate neural network directly on the ABI data would have been preferred, it was not possible due to missing overlap with the manual classifications. Nevertheless,

Table 2

Number of Time Windows That Contain Robustly Identified Patterns in the Boreal Winters of 2017/2018 (JFM), 2018/2019 (NDJFM), and 2019/2020 (NDJFM)

pattern	# of 6 h windows	% of total	% of robust patterns
Sugar	145	9	22
Gravel	305	19	46
Flowers	77	5	12
Fish	141	9	21
Others	846	58	N/A
mixed	567	36	
no pattern	337	21	

the channels of MODIS (channel 31; 10.78–11.28 μm) and ABI (channel 13; 10.18–10.48 μm) used here are relatively close to each other and in a wavelength range where absorption due to water vapor is relatively constant and overall minor. Differences are therefore expected to be minimal. A comparison of the overall performance of the visual classifications used in Rasp et al. (2020) to the infrared classifications used in this study is given in the Supporting Information.

While the GOES-16 ABI can capture images every minute for pre-selected regions, here we extract the region of interest (10°N , 24°N ; -61°E , -40°E) from the full-disk scenes and restrict ourselves to a temporal resolution of 30 min and the nominal spatial resolution of 2 km. Because the GOES-16 satellite only recently started its operation, we restrict our analysis to the three boreal winter seasons 2017/2018 (JFM), 2018/2019 (NDJFM), and 2019/2020 (NDJFM).

To attribute one of the four patterns to the observations made at the BCO, each classification of the neural network is evaluated at the location of

the observatory. Because the RetinaNet is an object-detection algorithm, classifications can overlap or contain cloud formations that are less characteristic of the main identified pattern. As we wish to include only clear and long-lasting patterns, while still keeping a statistically robust sample size, the complete time-series is split into 6 h time windows which are associated with a specific pattern in cases where a pattern dominates this time window for example, is detected for at least half of the time (3 h). This results in 42% of the 6 h windows being associated with one of the four patterns, while another 37% could not be attributed clearly to any category, only in 21% of the cases was no pattern detected for 3 h. Because the patterns are not equally likely to occur, the number of detected cases differs as indicated in Table 2. Time windows that do not contain a long-lasting pattern were grouped together as Others.

For the detection of the seasonal cycle of the patterns and the trajectory analysis we do not need to have high temporal sampling. Hence, we use the daytime MODIS AQUA overpass to identify patterns which allows us to extend the record to 11 years (2010–2020).

2.2. Back-Trajectories

To analyze the origin of the patterns and the evolution of the air mass in which they are found, we calculate back-trajectories following the framework of Eastman and Wood (2016). Vertical winds are assumed to be negligible compared to the horizontal components, such that the trajectories are followed near the top of the sub-cloud (boundary) layer and kept constant at the initial height of 925 hPa. These boundary-layer trajectories are calculated using winds from the fifth European Center Reanalysis of meteorological observations (ERA5) (Hersbach et al., 2020) on a 6-hourly time step.

The back-trajectories are initialized at the center of each classification within the domain 10°N – 24°N and 61°W – 40°W and most closely to the AQUA overpass time. The analysis covers the winter months (November through March) of 2010–2020. Trajectories are calculated for an 84 h period and atmospheric properties along the trajectory are extracted at each 12 h time-step coinciding with an AQUA overpass. Reanalysis variables are taken from a 1×1 degree latitude-longitude grid, with averages produced for all boxes with centers that fall within 100 km of trajectory sampling points.

2.3. Ground-Based Measurements

We use surface observations from the BCO. The only long-term cloud observatory in the broader trades.

2.3.1. Instrumentation

The BCO uses advanced remote sensing instrumentation to measure the undisturbed marine subtropical atmosphere (Medeiros & Nuijens, 2016; Stevens et al., 2016). In this study, we use simultaneous measurements from the CORAL Ka-band cloud radar and Raman lidar to characterize clouds and their thermodynamic

environment, especially the surrounding humidity structure of the clouds. These advanced remote-sensing measurements are complemented by 752 soundings of the nearby Grantley-Adams airport to improve the statistics above clouds, which can quickly attenuate the lidar signal and make a retrieval inside and above clouds impossible. Radiosondes are launched once or twice a day, usually an hour or so before their 0 UTC and 12 UTC report times. The closest of these soundings has been attributed to each of the 6 h time windows.

To detect only hydro-meteors with the cloud radar and no sea-salt aerosols, we apply a threshold of -50 dBZ as used in Klingebiel et al. (2019).

Integral measurements of liquid water path (LWP) and total integrated water vapor (IWV) are retrieved from microwave radiometer measurements following Löhner and Crewell (2003) and Steinke et al. (2015).

In addition to the standard surface meteorological measurements from a Vaisala WXT-520, we use the rain rate measurements from a micro-rain radar (MRR). Due to its larger sampling area compared to the also available acoustic rain sensor, it detects more reliable light (0.01 mm h^{-1} (Peters et al., 2002)) and/or short rain events. However, this comes at the cost of measuring the rain rate above the surface (325 m) rather than at the surface — which will be larger than at the surface, disproportionately so for light rain.

These datasets are available for 90% of the 6 h time windows and are equally distributed among the patterns. The only exception is the radiometer data with only about 60% availability.

2.3.2. Cloud Entity Classification

The identifications of meso-scale patterns of shallow convection are supplemented with cloud-type classifications derived from the BCO measurements.

Cloud-geometric properties of single cloud entities are retrieved based on the segmentation of the radar reflectivity. Individual clouds are identified by testing the connectivity of radar retrievals in height and time. Since a main part of this study focuses on stratiform layers, we use a running window of 100 s in time and only direct connections in the vertical to account for the fact that the stratiform layers can be so thin that they are not continuously detected by the radar.

Similar to Lamer et al. (2015) we classify individual clouds by their cloud-base heights (CBH). Stratiform layers are defined as clouds that have a frequent CBH above 1 km up to 2.5 km. As shall be seen later (Figure 3) the echo fraction minimizes at 1 km and therefore a threshold of 1 km separates best the stratiform cloudiness from the cloud layer below. This layer of clouds with CBHs below 1 km we classified as originating from the cumulus gene. An example of the radar reflectivity and the derived cloud-type classifications is shown in Figure 1. It illustrates that also a mixture of cumulus with an attached stratiform layer may exist. These cases are actually classified as “*StSc + Cu*” in the case the stratiform layer lasts for at least 20% of the time it takes for the cumulus cloud-entity to pass over the observatory.

Based on the single cloud entities, geometric properties like stratiform extent and mean thickness of stratiform layers are calculated and associated with each entity.

3. Surface Based Characterization of Cloudiness and Precipitation

The four patterns identified by Stevens et al. (2020) — *Sugar*, *Gravel*, *Flowers*, *Fish* — are purely defined by their visual impression from space, predominantly the spatial distribution of cloudiness. The cloudiness is therefore the physical quantity closest to the definition of these patterns. Among the physical differences that may accompany these patterns, aspects of cloudiness that go beyond the spatial arrangement of reflectivity as seen from above will be important to characterize, especially in so far as it influences the cloud radiative effect.

An overview of these patterns and the ground-based observations linked to them is shown in Figure 2. Differences in cloudiness are readily apparent, and conform to what has been previously noted in the literature. *Sugar* is identified with a fine dusting of clouds, *Gravel* with cloud features arranged around arc-like structures. *Flowers* and *Fish* are composed of elements that are yet larger in scale and show a clearer separation

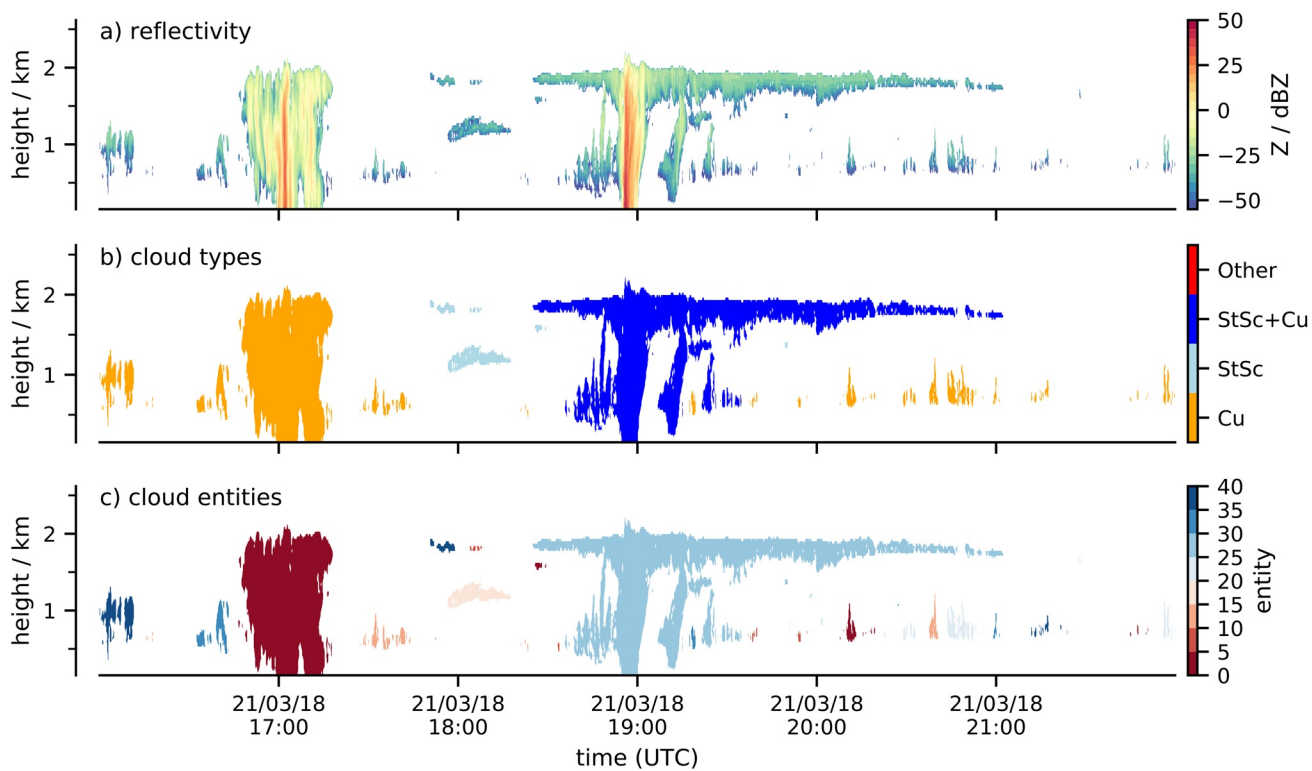


Figure 1. Example of cloud-type classification based on radar reflectivity.

between cloudy and clear-sky areas. For *Flowers* the clouds show a more isotropic distribution, while they are usually elongated—roughly West to East—in the case of *Fish*.

From these illustrations, which add to the examples shown in Stevens et al. (2020), it is natural to develop preconceptions about differences in the three-dimensional structure of the boundary layer associated with the patterns. For example, *Gravel* is generally thought to be associated with precipitation due to the visible cold-pool signature in the cloud field, and *Flowers* are thought to be composed of stratiform clouds with suppressed convection around them. Assessing whether such preconceptions are supported by the data, is one of the goals of this section.

We first focus on the characteristics of the cloudiness in terms of their geometric properties. Thereafter we analyze the precipitation signatures of the patterns, as they might help to gain a process understanding on how these different patterns form.

3.1. Cloudiness

The cloud cover at the BCO is shaped by the ubiquitous appearance of cumulus humilis—that is, cumulus clouds of very limited vertical extent. Cumulus humilis are not the only cloud type measured at the site. Even in the northern hemispheric winter, when the Intertropical Convergence Zone is furthest away from Barbados and the region experiences strong subsidence, the measured cloud fraction is not solely caused by non-precipitating cumulus humilis (Riehl, 1954). This is demonstrated by an analysis of the mean radar echo fraction profile (a combination of cloud- and rain-fraction) shown in Figure 3. Echoes are detected extending to depths above 3 km.

Looking at the mean echo fraction profiles of *Sugar*, *Gravel*, *Flowers*, and *Fish* and also the overall winter-time mean echo fraction, suggests that all but *Fish* are some form of shallow convection, with very small echo fractions (less than 3% at 4 km) extending much above 2.5 km.

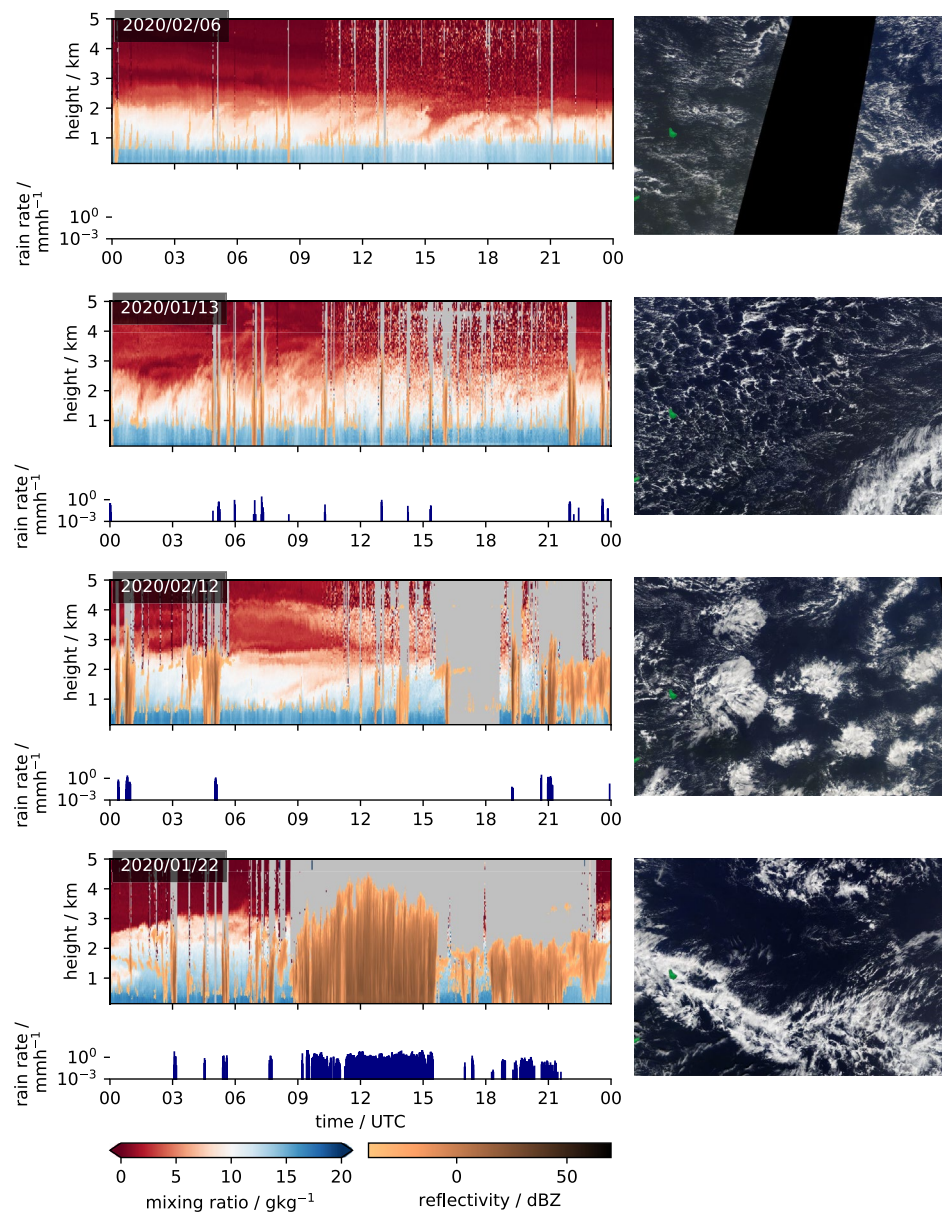


Figure 2. Time-series of each cloud pattern as identified by scientists participating in the EURECA campaign (top to bottom: *Sugar*, *Gravel*, *Flowers*, and *Fish*). Water vapor measurements from the Raman lidar overlaid by radar reflectivity shown in upper panels, while rain rates measured at 325 m are shown in the lower panels. The according Moderate Resolution Imaging Spectroradiometer images from the TERRA satellite overpass are shown on the right. Missing values are colored gray.

The largest inter-pattern variability in echo fraction is found in the layer between 1.5 km and 2.5 km. At 1.7 km echo fractions vary between 5% and 20% and explain a large part of the differences that give rise to the differences seen in the satellite imagery (e.g., Figure 2). For instance *Flowers*, with its cloudy patches of high reflectivity paired with the sheet-like structure anticipate a strong stratiform component in the cloud fraction compared to *Sugar* and *Gravel*, as is evident in the echo-fraction profiles. The overall echo fraction of *Flowers* (0.47) is therefore much more influenced by the stratiform cloud component as compared to *Sugar* (0.24) and *Gravel* (0.34). *Fish* has high echo-fractions throughout the cloud layer, but are less obviously dominated by a stratiform component as compared to simply more cloudiness, which often extends much more deeply through the lower troposphere.

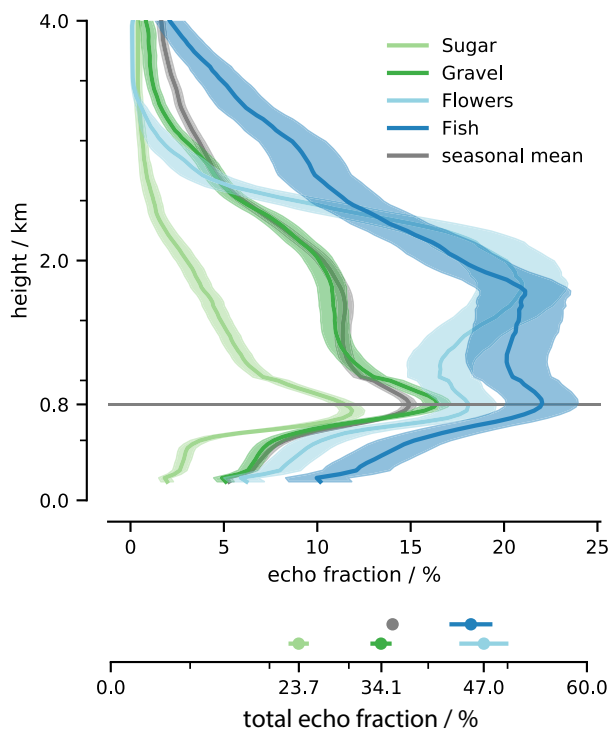


Figure 3. Echo-fraction measured at the Barbados Cloud Observatory (BCO) and grouped by detected pattern indicating the combination of cloud- and rain-fraction (upper panel). The height integral, total echo fraction, is shown in the bottom panel. The overall mean of the analyzed winter seasons is shown in gray with the height of maximum echo fraction shown as horizontal line. Shading and whiskers indicate standard error of mean.

Common to all patterns is the similarity in difference between the echo fraction at the surface and 700 m, which we interpret as the cloud base cloud fraction. The inter-pattern variations in echo-fraction at 700 m that do exist in Figure 3 can largely be attributed to rain events, that is, differences below 500 m — which are a signature of precipitation — are similar to those at 700 m. The lack of variability of cloud amount at the CBH was emphasized by Nuijens et al. (2014). That *Flowers* would have a similar echo fraction at cloud-base as *Sugar* when neglecting the rain contribution to the echo fraction was not something we would have guessed from the satellite imagery. It shows that an abundance of clouds near cloud-base under the cloud shield compensates for an absence of shallow-cloudiness in the cloud-free part of the *Flowers* pattern.

Looking at the cloudiness of the patterns as a whole, we recognize that the echo fraction of *Gravel* has the strongest similarity to the seasonal mean echo fraction, which is the average of all 6 h windows independent of any pattern. This is consistent with *Gravel* being the most common pattern detected in this study (about 19% of all regarded time windows and 45% of the windows with any dominant pattern). Furthermore, it also suggests that a large portion of the more uncertain and mixed time-windows contains cloudiness similar to the *Gravel* pattern. *Sugar*, in contrast, occurs rather seldom with 9%. This might seem to contradict Rasp et al. (2020) who found that *Sugar* is actually more often identified than *Gravel*. However, similar to Stevens et al. (2020), who were looking for dominating patterns on a fixed domain, we look for dominating patterns within a fixed time-period. Both methods register only patterns that are persistent for a long time or cover a large area, both of which de-emphasize *Sugar*. The cloud pattern with randomly distributed clouds of little vertical extent occurs frequently, but is often not dominant and thus not picked out by our analysis.

Figure 4 confirms that the differences in echo fraction at the lifting condensation level and below are indeed caused by different contributions

at the higher end of the reflectivity spectrum (>0 dBZ) which is indicative of precipitating hydro-meteors. Much more similar across patterns is that the vast majority of hydro-meteors are found at the lower end of the reflectivity spectrum. While the reflectivities below -50 dBZ close to the surface are characteristic for hygroscopically grown sea-salt particles (Klingebiel et al., 2019), with increasing height and reflectivity (toward -15 dBZ at about 2 km) the imprint of non-precipitating cumulus humilis (Lonitz et al., 2015) is found.

Despite a similar cloud cover for both *Flowers* and *Fish* of about 0.5, Figure 4 indicates different relationships between the cumulus and the stratiform cloud layer. Whereas *Flowers* show a second distinct reflectivity maximum at about 2.2 km and near -5 dBZ, the distribution is more monomodal for *Fish*. This two-layer

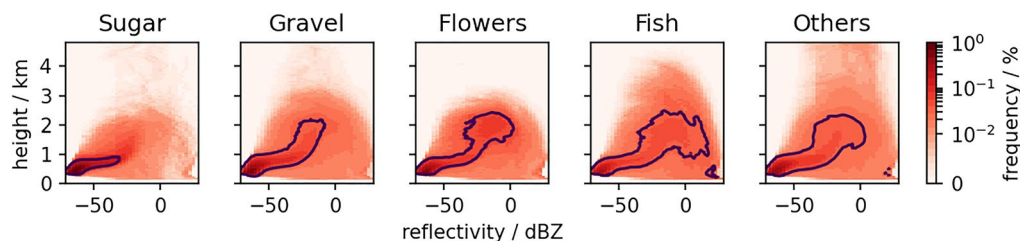


Figure 4. Contoured frequency by altitude diagram (CFAD) for the four patterns of shallow convection and less clear patterns gathered in the group *Others*. The colors indicate the frequency of occurrence of a reflectivity-height tuple within a specific pattern. The tuples explaining 50% of all values are contoured in black. Hydrometeor-free profiles are excluded.

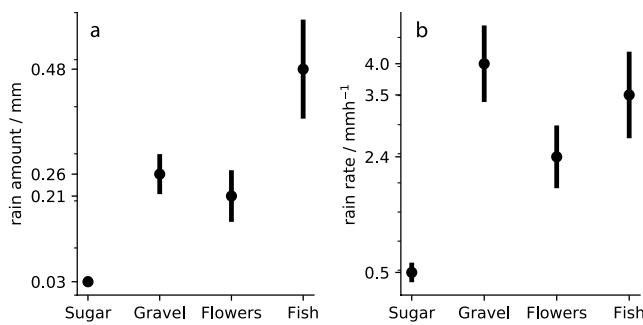


Figure 5. Rain statistics of each pattern averaged over a 6 h period. The average rain amount (left) and the average maximum rain rate of each window (right) are shown with their standard error.

structure suggests that *Flowers* are only sporadically connected by higher cumulus convection whereas for *Fish*, clouds aloft appear to be deeper and as a more continuous extension of clouds near cloud base. More like the more active and deeper distribution of *Gravel*. The deeper echoes for *Fish* are also evident in a stronger precipitation feature (i.e., 25 dBZ near surface mode).

Looking at single entities of the clouds detected within the classified 6 h analysis periods as described in Section 2.3.2, we found no evidence that these different couplings of the stratiform cloud layer to the underlying cumulus convection influences the geometric properties of these layers. Independent of the meso-scale organization, cumulus coupled stratiform layers (*StSc + Cu*) have a CBH between 980 and 1050 m and a cloud top height between 1240 m and 1370 m. More broadly, any of the individual cloud components differentiated here: stratus (*StSc*), cumulus (*Cu*) and the connection of both/stratocumulus cumulogenitus (*StSc + Cu*) show similar geometric properties independent of the pattern.

The CBH of cumulus, which to a first approximation is the same as the lifting condensation level of near surface air, is at about 650–700 m with cloud tops about 160 m higher. Stratus are about 130 m thick on average, with an average CBH between 1600 m and 1850 m, which is somewhat higher than for stratiform layers that are connected to a convective core during the time of observation.

The only differences that do exist, are the lack of stratiform layers in case of *Sugar* and the increase in size of the stratiform components (*StSc; StSc + Cu*) from *Sugar* (3 km; 10 km) via *Gravel* (5 km; 27 km) to *Fish* (7 km; 63 km) and *Flowers* (11 km; 55 km). The 95th percentile is given in brackets as this can be assumed to better capture the characteristic length of the stratiform cloud decks by excluding very small entities and entities whose path length is much smaller than the actual characteristic length as the observatory rarely samples the clouds at their characteristic cross section. The translation from cloud entity length in time to space has been done by using the wind speed at cloud height measured by the nearest sounding.

3.2. Rainfall

To assess, how important precipitation might be for different patterns, we characterize its frequency and strength in the following. From the example time-series shown in Figure 2 and the results from the previous section, we expect a clear separation of the precipitation characteristics among the patterns: from the lack of rain during the occurrence of *Sugar*, to frequent showers in the case of *Gravel*, to yet stronger rain events for *Fish*.

To test this expectation, we analyze at the precipitation measurements from the BCO within the same 6-h time windows used in the section above. First, we quantify how many analysis windows contain any rain event. With the exception of *Sugar*, in more than 50% of the identified cases, rain is present. For *Sugar* precipitation can be detected in only 35% of the cases.

This absence of rain events in case of *Sugar* is even more evident in the quantification of the mean near-surface rainfall (Figure 5a). Rain amounts are similar for *Flowers* and *Gravel*, consistent with the frequency of near surface echoes evident in Figures 3 and 4, nearly twice as large for *Fish*. We also quantify rain intensity by averaging the maximum rain-rates within each analysis window for each of the patterns. Among the precipitating patterns rain intensities do not differ as substantially. In all of these cases the precipitation is intense (approach 10 cm a day), and well above the threshold (1 mm h^{-1} to 2 mm h^{-1}) that past studies have associated with the formation of cold-pools (Barnes & Garstang, 1982; Drager & van den Heever, 2017).

By applying the threshold of 1 mm h^{-1} to the maximum rain events, the number of cases with significant rainfall decreases to 12% in case of *Sugar* and about 35% for the other patterns. 35% might not seem to be a lot, but it has to be kept in mind that these patterns are of meso-scale extent and even a 6 h-period cannot capture the complete variability. This is especially the case for the *Fish* pattern, where a 6 h-period

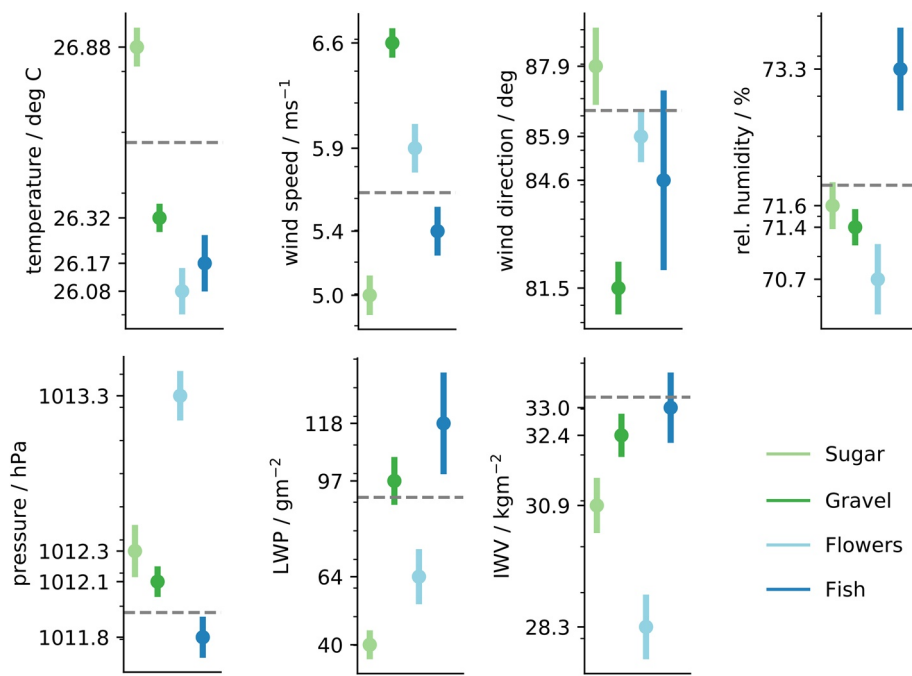


Figure 6. Surface meteorology measured at the Barbados Cloud Observatory during the observation of the four patterns. The seasonal mean of the observed time-period independent of any pattern is drawn as gray line.

might only capture the clear-sky part of the *Fish* and therefore the importance of precipitation may be underestimated.

Our data do not contain sufficient samples to evaluate to what extent the spatio-temporal characteristics of precipitation differs among the patterns. However, by analyzing the precipitation signature in all 138 6-hourly windows of *Fish*, there is evidence of a bimodal distribution of rain events, with a second mode consisting of extended periods of precipitation (like the one shown in Figure 2) that is, not evident for either the case of *Flowers* or *Gravel*.

Overall, precipitation events of significant strength occur during *Gravel*, *Flowers* and *Fish* periods and suggest that precipitation plays a role in the patterning process, or at least in the persistence of these patterns. There is no hint that precipitation is important for *Sugar*.

4. Meteorological Environment

In the previous section we characterized similarities and differences in cloud- and precipitation-signatures among the four patterns. To the extent the patterns are forced, this forcing might be evident in the local meteorological setting. In this section, we address this possibility and investigate the meteorological settings, first at the surface and then within the free troposphere, for the different patterns.

4.1. Surface Measurements

Near surface (5 and 25 m above mean sea level) meteorological measurements at the BCO are composed by pattern in Figure 6. Common to all variables shown is a distinguished value for at least one of the patterns.

Sugar distinguishes itself from other patterns by virtue of its mean temperature and low wind-speed. Given that annual cycle of surface temperatures is just over 2 K this 0.6 K difference is large. While *Sugar* is associated with unseasonably warm conditions, the contrast with the other patterns is due in equal part to them being unseasonally cool, which is consistent with *Sugar* arising during periods with little northerly contribution to the mean flow. *Gravel* is distinguished by the surface winds being unseasonably strong and northerly. *Flowers* are found on the days that are coolest, when surface winds are strong, but not so strong

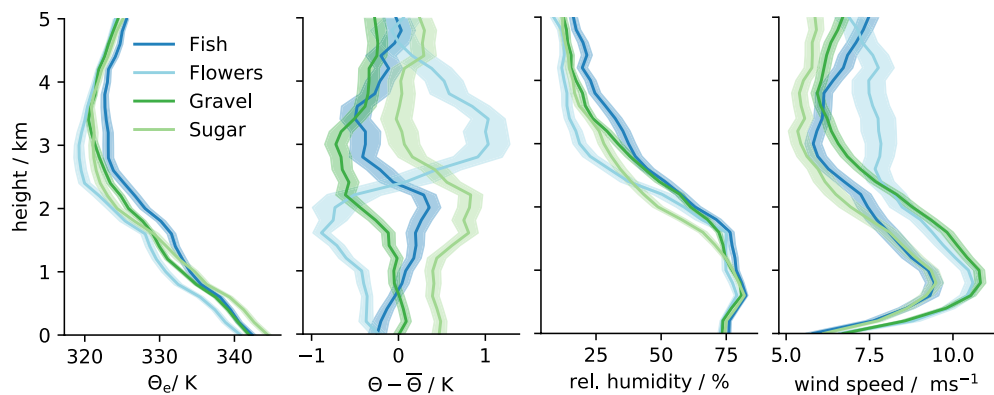


Figure 7. Average profiles of equivalent potential temperature, potential temperature difference to the overall pattern mean, relative humidity and wind speed from soundings at the Grantley Adams Airport (standard error is shaded).

as for *Gravel*, and when the surface pressure is unseasonally high (1,013.3 hPa). In contrast *Fish* which are also associated with extensive cloud coverage (Figure 3) are found on days with unseasonally low pressure (1,011.8 hPa), high humidity and relatively low but quite variable (in terms of direction) winds, consistent with more disturbed conditions and extended periods of precipitation.

Amongst all analyzed surface observations, wind speed is the best proxy for a specific pattern. The lowest mean wind is measured during *Sugar* situations with 5 m s^{-1} . For the other patterns the mean wind speed increases by an increment of 0.5 m s^{-1} from *Fish* to *Flowers* to *Gravel*. The finding that *Flowers* and *Gravel* occur in conditions of higher winds is consistent with what was found by Bony et al. (2020), but further discriminates among all patterns rather than two groupings (e.g., *Flowers* and *Gravel* as high wind-speed and *Sugar* and *Fish* as low wind-speed patterns). This suggests that there may be processes that are not captured by the reanalysis, especially so as we gain similar results to Bony et al. (2020) when compositing the ERA5 surface data (Figure S4).

4.2. Vertical Structure

The previous analysis is extended in the vertical through a composite analysis of the Grantley Adams radiosonde data. The pattern mean-soundings, and their associated uncertainty estimates, are presented in Figure 7. Composites are made of the equivalent potential temperature, potential temperature difference ($\Theta - \bar{\Theta}$, where $\bar{\Theta}$ is the mean sounding across all patterns), relative humidity and wind speed.

Surface temperature differences measured at the BCO are also evident in the soundings, and extend through the depth of the moist (lower 3 km) layer. *Flowers* distinguish themselves not only by lower surface temperatures, but also by a much stronger stratification atop the humid layer, showing a strong inversion at about 2.5 km. *Sugar* appears associated with a much shallower cloud layer, also capped by an inversion. The apparent instability (decrease in $\Theta - \bar{\Theta}$ with height) for the other patterns simply indicates that they are less stable on average. The lower-tropospheric stability (LTS) is $16.2 \pm 0.3 \text{ K}$ in case of *Flowers* and nearly 2 K lower for *Fish* ($14.7 \pm 0.2 \text{ K}$), *Sugar* ($14.4 \pm 0.2 \text{ K}$) and *Gravel* ($14.1 \pm 0.1 \text{ K}$). However, in case of *Sugar*, the value of Θ at 700 hPa (which is used to construct LTS) may miss the shallow stable layer that appears to cap the convective development of this pattern.

The relative humidity profile is strongly coupled to the convective activity and hence the echo fraction (e.g., Figure 3) As we have shown in the last section, *Sugar* is mostly characterized by cloudiness at CBH with few clouds reaching up to 1.8 km. In agreement, the according moisture profile shows a shallower layer compared to the other patterns that more regularly reach the inversion height and distribute moisture. Likewise *Fish*, with echos reaching more deeply through the lower troposphere is also considerably moister than the other patterns above 3 km. These humidity profiles also help explain differences in θ_e , particularly in the upper cloud layer and lower free-troposphere. For example, as seen by contrasting *Fish* and *Gravel*.

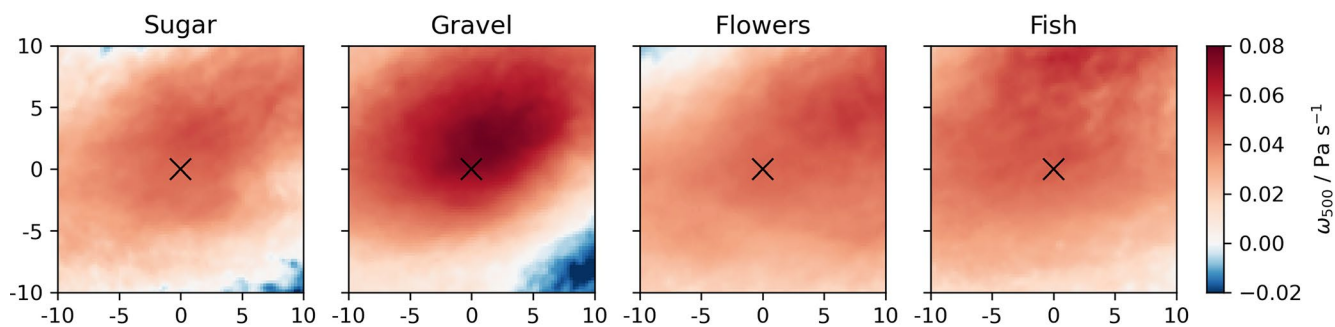


Figure 8. Distribution of subsidence strength ω_{500} relative to identified pattern centers composited by $20 \times 20^\circ$ domains around each identified pattern. Pattern centers are marked with a cross.

Based on measurements made during RICO, Nuijens et al. (2009) analyzed differences in θ_e similar to those shown in Figure 7. Consistent with their findings these profiles seem to co-vary consistently with surface wind speeds. Stronger surface winds for *Gravel* and *Flowers* are mostly confined to the moist layer for *Gravel*, but extend through the lower troposphere for *Flowers*. These winds are one component of what is often thought of as an externally imposed large-scale forcing, to which the boundary layer thermodynamic profiles relatively quickly equilibrate.

4.3. Large-Scale Forcing

We use ERA5 data in a $20^\circ \times 20^\circ$ domain centered around each ABI classification to examine how the large-scale subsidence (ω_{500}) varies as a function of pattern. Those domains are afterward averaged to one composite that shows the strength of subsidence at the center of each pattern, but also in its surrounding.

Figure 8 reveals that all patterns occur during times of subsidence and that this subsidence is in most cases also similar to the typical subsidence rate of 0.05 hPa s^{-1} in the Atlantic trade-wind regime (Holland & Rasmusson, 1973). However, it also shows that some variability in the large-scale forcing exists and stronger subsidence is, contrary to expectation, not occurring during *Sugar* and *Flowers* cases, but rather during *Gravel* cases (Table 3).

In the subtropics, particularly in association with stratocumulus, subsidence co-varies positively with LTS. On shorter time scales and deeper in the tropics, other factors may play a role. In particular the temperatures above the cloud layer are tightly coupled to moisture, so as to homogenize the density temperature on isobaric surfaces. This partly explains the stronger temperature inversion for *Flowers*. It also means that boundary layer variability may play a more important role in determining the LTS, consistent with near-surface temperature differences as illustrated in Figure 6.

5. Are the Four Patterns Indicative of Specific Air Masses?

Rasp et al. (2020) showed that globally, the four patterns predominate in the dry tropics, regions often associated with the trade winds. The analysis in the previous section identified subtle differences in the environments in which the four patterns form. This raises the question as to the origin of these environmental differences, that is, to what extent they arise from subtle variations within the trades, or what one might alternatively think of as disturbances to or departures from canonical trade-wind conditions. We explore this question by analyzing the seasonal cycle of the four patterns within our North Atlantic study region as well as the air-mass histories of the different patterns by compositing reanalysis data along back-trajectories constructed from that same data.

Table 3
Large-Scale Forcing Averaged by Pattern From Fixed-Location Sounding Data (Snd) and ERA5 Data From Pattern Center

Pattern	LTS _{Snd} (K)	LTS _{ERA5} (K)	$\omega_{500, \text{ERA5}}$ (Pa s ⁻¹)	freq. of convergence (%)
Sugar	14.3	14.8	0.046	28
Gravel	14.0	14.4	0.072	38
Flowers	16.2	16.6	0.046	34
Fish	14.6	16.0	0.048	59

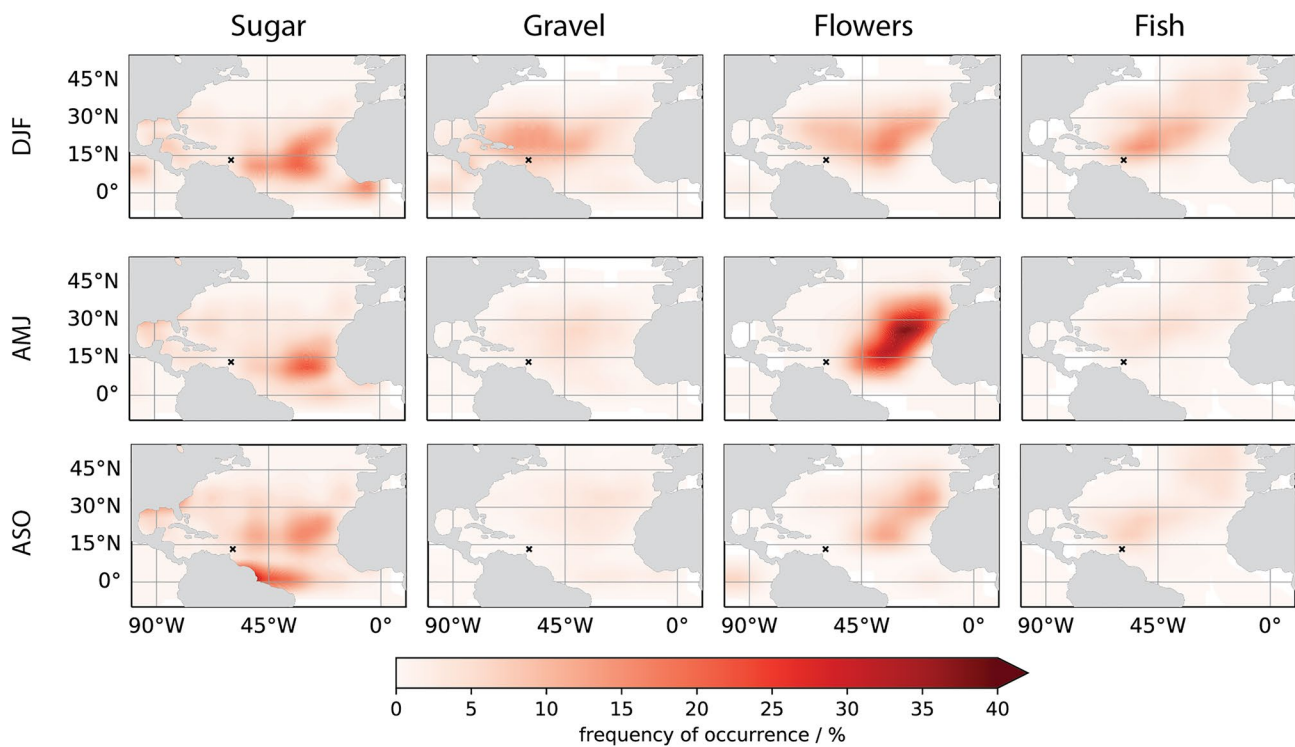


Figure 9. Seasonal distribution of patterns in the North Atlantic in the dry- (December-January-February [DJF]), transitional- (April-May-June [AMJ]) and wet- (August-September-October [ASO]) season (top to bottom) detected in infrared imagery (AQUA Moderate Resolution Imaging Spectroradiometer (MODIS) 2010–2020).

5.1. Seasonality

Considering just the region of the downstream trades, taken to be the tropical North Atlantic west of 45° W, most patterns predominate in the boreal winter trades as shown by Figure 9. *Fish* and *Gravel* seem only to occur in this region in conditions (DJF) when the trades are well developed. *Flowers* are also present in boreal spring and early summer (AMJ). *Sugar* shows very little seasonality. Rather, and consistent with the analysis by Rasp et al. (2020), it appears associated with suppressed conditions bordering the ITCZ whose seasonal migration it follows. Based on this we hesitate to call *Sugar* a trade-wind cloud pattern.

Flowers are even more common in the “upper” trades (east of 45° W), even more so in the April-June period, (e.g., Figure 9). Such a distribution is consistent with an affinity for conditions that favor stratocumulus. This distribution is in agreement with the analysis in the previous section, which showed that *Flowers* favor conditions of higher lower tropospheric stability, and lower surface temperatures, as compared to the other patterns. This supports the idea that *Flowers* are the downstream manifestation of the familiar, but much smaller, closed cellular stratocumulus (Stevens et al., 2020); alternatively, it may be indicative of a failing of the neural network in the upper trades because it has not been trained to distinguish between the very similar looking *Flowers* and closed-cells.

5.2. Lagrangian Evolution of Air Masses by Meso-Scale Organization

Here we use the back-trajectories, initialized at the center of the MODIS AQUA classifications following the boundary layer winds at 925 hPa for 84 h, to investigate possible reasons for the environmental differences associated with each pattern as described in Section 2.

Figure 10 shows that the back-trajectories are consistent with the steadiness that characterizes the winter trades, with the trajectories aligning well along the general flow of the trades as they come to their point of initialization. They do however differentiate themselves as one follows their history back in time. Most

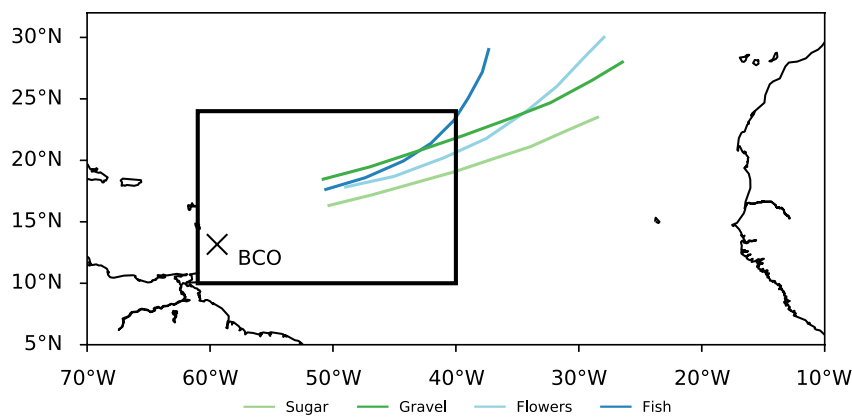


Figure 10. Mean back-trajectories for the different patterns initialized at the center of individual classifications within the indicated black box at 925 hPa and calculated for 84 h.

notably *Fish* which originates far to the west of the other trajectories. A more tropical influence on *Sugar* is also consistent with its back-trajectories which start furthest south.

Compositing the large-scale conditions on the trajectories shows that many of the environmental differences previously documented are apparent well in advance (and upstream) of where the pattern was eventually identified (Figure 11). *Sugar* has warmer sea-surface temperatures, weaker winds and a relatively moist free-troposphere along its entire back-trajectory, consistent with a more tropical influence. *Flowers* evolve over cold ocean temperatures throughout the trajectory paired with persistently high LTS (despite rising SSTs), a dry free troposphere and stronger low-level winds. And differences in LTS among the patterns are robust and in place already 48 h earlier.

The time-evolution of different fields is also indicative of dynamic influences. For instance, for *Flowers* an acceleration of the low-level winds between -24 and -48 h may be driving the strong subsidence at 700 hPa, which in turn would support the already anomalously dry free-troposphere to dry further and increase the LTS. This pattern preceding process may drive the differences between *Flowers* from *Gravel* with the slight slackening of the winds and the decrease of the subsidence nearer the time and place where the pattern is identified, playing less of a role. In contrast, for *Fish* a strong temporal evolution within the last 24 h, as manifest through a moistening of the lower troposphere, might be indicative of a dynamic distur-

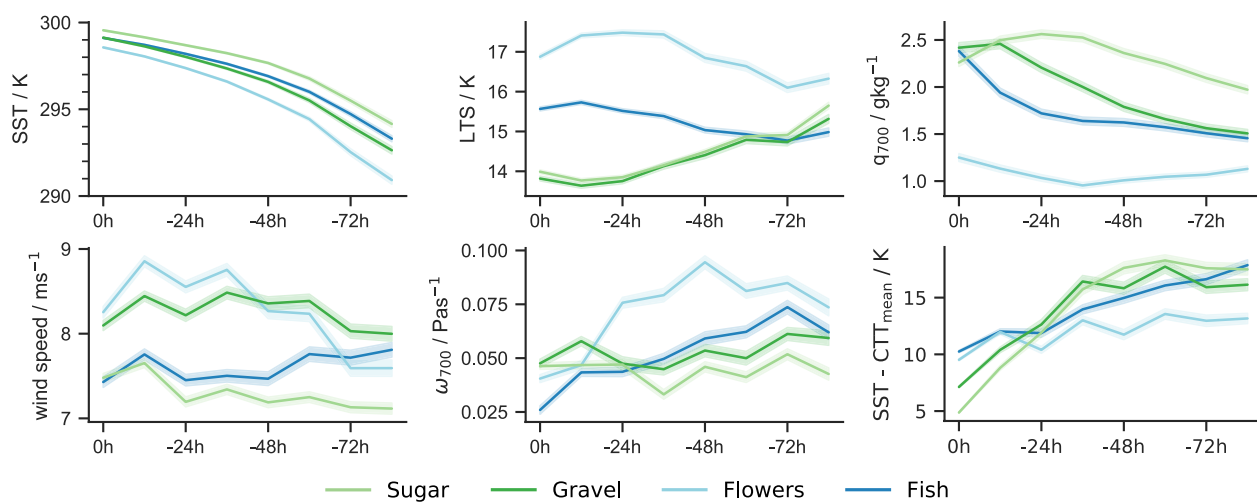


Figure 11. Environmental conditions along the back-trajectory of air-masses before time of pattern detection. All values are ERA5 reanalysis properties, except the cloud top height estimate where the cloud top temperature (CTT) is sourced from Moderate Resolution Imaging Spectroradiometer AQUA observations. Shading indicates standard error.

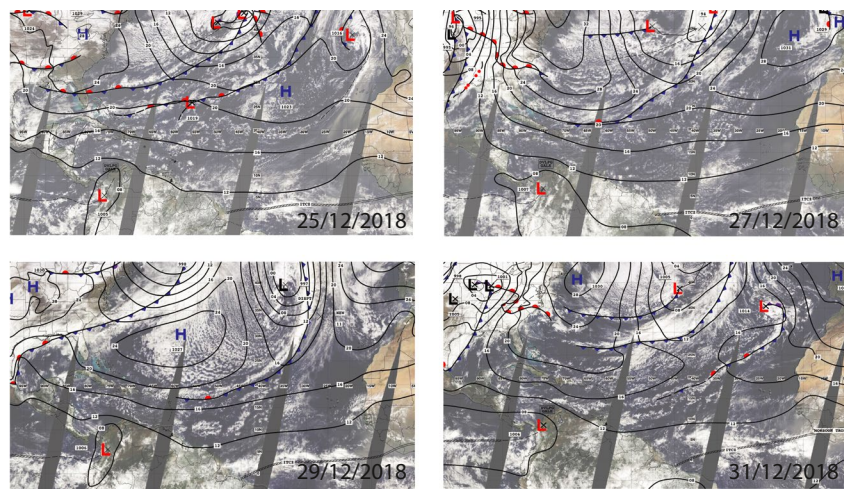


Figure 12. Cold air outbreak between December 25, 2018 and December 31, 2018. Surface analysis charts from the National Hurricane Center are adapted and overlaid on Terra Moderate Resolution Imaging Spectroradiometer images.

bance. *Sugar* seems less representative of a sudden stilling in the winds in association with local suppression, if anything recovering from more suppressed conditions and weaker winds upstream.

The time-evolution of cloud top height, estimated as the difference between the ERA5 sea surface temperature and the mean cloud top temperature sourced from MODIS within 100 km around the trajectory sampling point, can further be an indication of different lifetimes of the patterns. *Sugar* and *Gravel* seem to set up only shortly before the detection (~ 36 h) when the cloud top height dropped quickly, which would be indicative of a shorter lifetime. In contrast, *Flowers* and *Fish* might have persisted longer because the cloud top height evolves only little. It has to be kept in mind that this estimation of cloud depth is sensitive to high clouds that are filtered by the nature of the classification at the time of detection, but likely influence the CTTs further upstream. The changes of cloud depth might therefore appear magnified.

The diurnality that is, pronounced in a number of fields (wind speed, ω_{700} , SST-CTT) is explored in more depth by Vial et al. (2021).

5.3. Extra-Tropical Disturbances

Although we focus on the northern hemispheric winter season where the trades are well formed, disturbances to the trade-wind mean flow are well documented (Bunker et al., 1949; Riehl, 1945). The earlier literature identifies two types of disturbances, one associated with anomalously deep easterlies (which might be associated with active deep convection), the other associated with extra-tropical intrusions in the form of trailing cold-fronts from extra-tropical cyclones.

The older literature conceptualized the later (extra-tropical intrusions) as tropical incursions of the “polar front.” Especially in the boreal winter, when the Intertropical Convergence Zone is further south and the Azores high is less well established, frontal disturbances can extend equator-ward. By the time they reach the subtropics, their temperature signature is muted and they become most pronounced in the form of a shear line that separates the light easterlies from the stronger north-easterlies (Riehl, 1945).

Such a frontal passage can be seen in the surface analysis charts for example, in association with a deepening cyclone over the mid-Atlantic (near 45°N and 45°W) on December 25, 2018. Through the course of six days the cold front, initially supported by the outflow of cold-continental air (a cold air outbreak) from the east-coast of North-America, occludes upon reaching the tropics as far south as Barbados (see Figure 12).

By comparing the surface analysis chart with the satellite image, we recognize that the front is visible as a band of convection that we would classify as *Fish*. In the former cold sector, just north of the front, one can

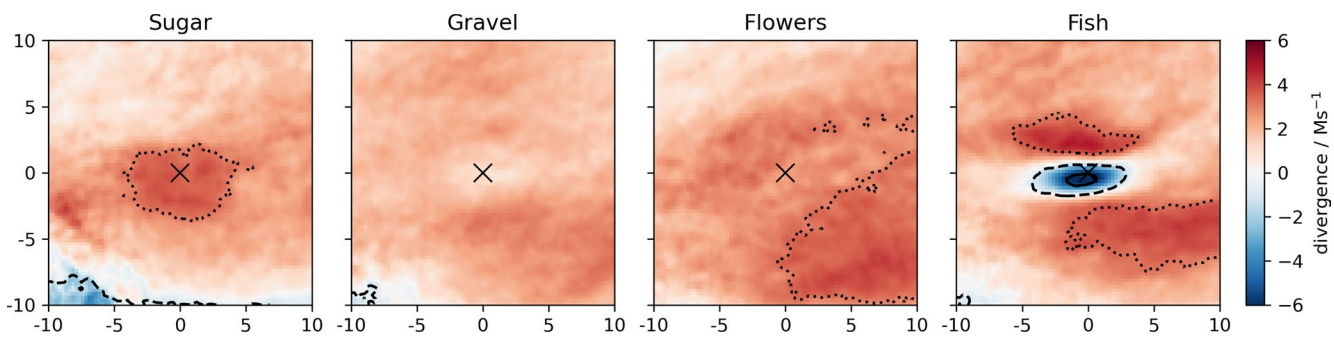


Figure 13. Distribution of divergence at 950 hPa relative to identified pattern centers composed by $20 \times 20^\circ$ domains around each identified pattern. Contours indicate frequency of events with convergence larger $1 \times 10^{-6} \text{ s}^{-1}$ (30%: dotted, 45%: dashed, 60%: solid). Pattern centers are marked with a cross.

also notice on December 29 cloud structures north of the front similar to *Flowers* (more pronounced to the west) or perhaps *Gravel*.

We repeat our composite analyses done to create Figure 8 with surface convergence to test, whether the frontal character is typical for *Fish* and whether other patterns can be related to the fronts as well. We find a signal of strong convergence ($>1 \times 10^{-6} \text{ s}^{-1}$) connected with *Fish* about 60% of the identified cases (Figure 13). A clear signature for the other patterns is less pronounced, although the absence of convergence for *Sugar* is consistent with it being more locally suppressed. For *Fish*, the pattern of convergence extends zonally in a way that supports the hypothesis of *Fish* arising in association with disturbances associated with trailing cold-fronts or shear-lines from extra-tropical intrusions.

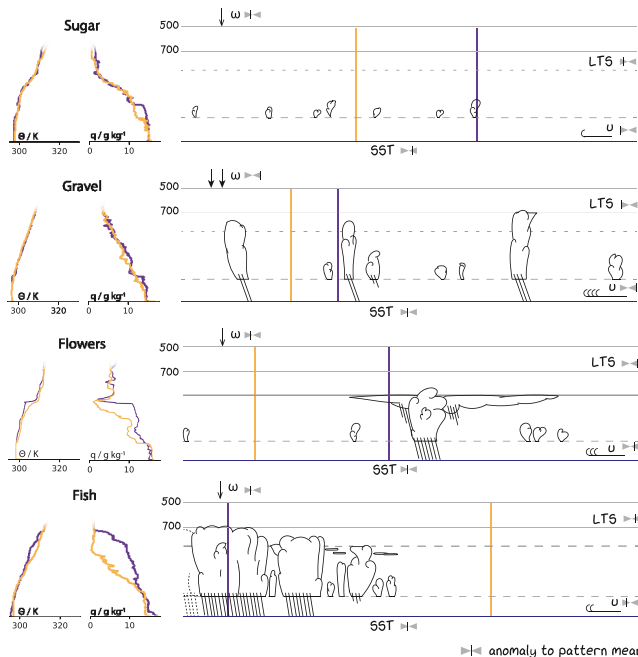


Figure 14. Illustration of the cloud field during the four patterns of meso-scale organization and the associated large-scale forcing (right) including the thermodynamic profiles (left). The anomaly in forcing to the pattern mean is indicated by gray sliders. Vertical lines indicate the contrasting positions of the thermodynamic profiles, purple being in the moist part and orange in the dry area. Thermodynamic profiles are based on soundings during the EUREC⁴A field campaign (Stephan et al., 2020).

6. Discussion and Conclusion

Cloud- and environmental properties associated with four patterns of meso-scale organization in the lower trades (50°W to 60°W) of the North Atlantic are examined. The four patterns follow the *Sugar*, *Gravel*, *Flowers*, *Flowers* taxonomy of Stevens et al. (2020) and are identified using a neural-network applied to high-resolution infra-red imagery from the GOES-16 and AQUA satellites.

We conditioned surface observations, back-trajectories, and reanalysis data on the identification of different patterns to answer three questions: One, do the four patterns show physical differences in the cloud geometry as seen by surface-based remote sensing? Two, can differences in the large-scale environment associated with different patterns be discerned? And, three can we identify the origins of discernible environmental differences among the patterns.

Figure 14 summarizes these results and illustrates that the four patterns differ in more than just their satellite presentation. Cloud coverage and its vertical distribution differ and differences in the environment of different patterns are discernible. The thermodynamic profiles in Figure 14 show inter-pattern differences, but also intra-pattern differences as measured by radiosondes at points whose position relative to other features within a pattern is schematized.

Many preconceptions from earlier studies, either inferred from snapshots (Stevens et al., 2020) or from compositing reanalysis data on values of a cloud-clustering index that correlate with different patterns (Bony et al., 2020), are supported by our analysis. As an example, *Flowers*, and to some extent *Fish*, have a stratiform component detectable from surface-based remote sensing. In the latter this is less distinctly a capping

stratiform, or stratocumulus layer, as it is associated with more cloudiness throughout the cloud layer. Compared to the mean conditions, or the other patterns, LTS is higher (0.5–1.0 K) for *Fish* and (2 K) for *Flowers*.

Non-precipitating cloud coverage at the lifting condensation level, as emphasized by Nuijens et al. (2014) for the entirety of trade-wind cloudiness, also holds across the four patterns. This came as a surprise given that *Flowers* and *Fish* are characterized in part by their cloud free areas. Differences in cloud-base echo fraction largely reflect differences in precipitation, suggesting that to the extent environmental conditions demand an increase in the mass flux out of the sub-cloud layer, for instance as shown by George et al. (2020), this is largely associated with the development of deeper clouds and precipitation.

Similar to what was found by Bony et al. (2020), near surface winds identify *Flowers* and *Gravel* with strong near-surface winds, and *Fish* and *Sugar* with light winds. Our analysis, further discriminates within these two groups, with *Sugar*, *Fish*, *Flowers*, and *Gravel* each being separated by a roughly 0.5 m s^{-1} increase in surface wind speeds. Precipitation increases with near surface winds, as previously noted for measurements during RICO (Nuijens et al., 2009), with *Fish* being an outlier whose large rain rates are associated with extra-tropical disturbances and anomalous low-level convergence.

Seasonal variations and back-trajectories provide further insight into the origin of differences in the environments of the different patterns. The view of trade-wind clouds as cumulus humilis, and hence non-precipitating with little vertical extent, as popularized by studies based on data from BOMEX (Siebesma & Cuijpers, 1995) and most closely associated with *Sugar* suggests that these are at least in the form of large-scale homogeneous areas rather uncharacteristic of the trades. *Sugar* is found to favor more suppressed conditions, uncharacteristically (for the trades) weak winds, and proximity to deeper convection in the ITCZ.

As a historical note, the third author recalls that when the large-eddy simulation community began focusing on shallow trade-wind convection through simulations of conditions derived from BOMEX data (Siebesma et al., 2003), Bruce Albrecht admonished us that less suppressed and more stratiform capped conditions — as for instance seen and simulated in association with the Atlantic Trade-Wind Experiment (Stevens et al., 2001, ATEX) and which we might today call *Flowers* — were more characteristic of the trades. We find confirmation for his point of view, twenty years later, in our data. Given the association of *Fish* with shear lines from remnant extra-tropical cold fronts intruding deep into the sub-tropics, only *Gravel* is left to add to *Flowers* as an archetypical form of trade-wind convection. *Fish* and *Sugar* are intruders.

Gravel and *Flowers* differ substantially in their cloud amounts (as seen here) and their cloud radiative effects, as shown by Bony et al. (2020). We attribute this to *Flowers* forming in conditions of weaker winds, and a drier and warmer free troposphere. These differences to *Gravel* would support a more pronounced capping inversion, and stronger boundary layer cooling. Based on back-trajectories we hypothesize that these conditions arise from an acceleration of the trades and stronger subsidence in the upstream flow along *Flowers* back-trajectories. This hypothesis lends itself well to tests with LES, and may even be evident at the somewhat coarser resolution now being simulated by a new generation of global storm-resolving models (Satoh et al., 2019).

Independent of the formation mechanism, understanding of the conditions favoring one or the other pattern may help anticipate to what extent climate change, by virtue of changes in wind-speeds, or the frequency of extra-tropical disturbances, or changes in the opacity and stability of the free troposphere, will affect the frequency of occurrence for different patterns, and thus cloud-radiative effects in the lower trades. The widening of the tropics (Seidel et al., 2008) and the poleward shift of the extra-tropical storm-tracks (Ulbrich et al., 2008; Yin, 2005) would, following our analysis, disfavor *Fish* and *Flowers* patterns in favor of *Sugar* with a much smaller cloud fraction, and less pronounced cloud radiative effects.

Data Availability Statement

Open Research Primary data and scripts used in the analysis and other supporting information that may be useful in reproducing the authors' work can be obtained from <https://doi.org/10.5281/zenodo.4767674>. The ERA5 datasets used in this study (Hersbach et al., 2018a, 2018b) have been provided by the Climate Data

Store. GOES-16 ABI Level 1b radiances are available at <https://doi.org/10.7289/V5BV7DSR> and were converted with (Raspaud et al., 2019) to brightness temperatures. MODIS imagery originates from the NASA Worldview application (<https://worldview.earthdata.nasa.gov>), part of the NASA Earth Observing System Data and Information System (EOSDIS).

Acknowledgments

The authors thank the members of the Tropical Cloud Observation group for maintaining the Barbados Cloud Observatory and fruitful discussions. The authors would also like to thank Jiawei Bao for helpful comments on an earlier version of this manuscript. The authors thank Minghua Zhang for his editorial contributions and three anonymous reviewers for their constructive feedback. Hauke Schulz and Bjorn Stevens acknowledge partial funding through the European Union's Horizon 2020 Research and Innovation Programme under grant agreement No. 820829 (CONSTRAIN Project). The work of Ryan Eastman was supported by NASA grant 80NSSC19K1274. Open access funding enabled and organized by Projekt DEAL.

References

- Barnes, G. M., & Garstang, M. (1982). Subcloud layer energetics of precipitating convection. *Monthly Weather Review*, 110(2), 102–117. [https://doi.org/10.1175/1520-0493\(1982\)110<0102:SLEOPC>2.0.CO;2](https://doi.org/10.1175/1520-0493(1982)110<0102:SLEOPC>2.0.CO;2)
- Bony, S., & Dufresne, J.-L. (2005). Marine boundary layer clouds at the heart of tropical cloud feedback uncertainties in climate models. *Geophysical Research Letters*, 32, L20806. <https://doi.org/10.1029/2005GL023851>
- Bony, S., Schulz, H., Vial, J., & Stevens, B. (2020). *Sugar, Gravel, Fish, and Flowers: Dependence of mesoscale patterns of trade-wind clouds on environmental conditions*. *Geophysical Research Letters*, 47(7), e2019GL085988. <https://doi.org/10.1029/2019GL085988>
- Bunker, A. F., Haurwitz, B., Bernhard, M., Starr, J., & Stommel, H. M. (1949). Vertical distribution of temperature and humidity over the Caribbean Sea. *Papers In Physical Oceanography And Meteorology*, 11(1), 82. <https://doi.org/10.1575/1912/436>
- Denby, L. (2020). Discovering the importance of mesoscale cloud organization through unsupervised classification. *Geophysical Research Letters*, 47(1), e2019GL085190. <https://doi.org/10.1029/2019GL085190>
- Drager, A. J., & van den Heever, S. C. (2017). Characterizing convective cold pools. *Journal of Advances in Modeling Earth Systems*, 9(2), 1091–1115. <https://doi.org/10.1002/2016MS000788>
- Eastman, R., & Wood, R. (2016). Factors controlling low-cloud evolution over the eastern subtropical oceans: A lagrangian perspective using the A-train satellites. *Journal of the Atmospheric Sciences*, 73(1), 331–351. <https://doi.org/10.1175/JAS-D-15-0193.1>
- Gaiser, H., de Vries, M., Lacatusu, V., vcarpani, Williamson, A., Liscio, E., et al. (2018). *Fizyr/keras-retinanet 0.5.0*. Zenodo. <https://doi.org/10.5281/zenodo.1464720>
- George, G., Stevens, B., Bony, S., Klingebiel, M., & Vogel, R. (2020). Observed impact of meso-scale vertical motion on cloudiness. *Journal of the Atmospheric Sciences*, 1–30.
- Hersbach, H., Bell, B., Berrisford, P., Blavatik, G., Horányi, A., Muñoz Sabater, J., & Thépaut, J.-N. (2018). ERA5 hourly data on single levels from 1979 to present. Copernicus Climate Change Service (C3S) Climate Data Store (CDS). <https://doi.org/10.24381/cds.adbb2d47>
- Hersbach, H., Bell, B., Berrisford, P., Hirahara, S., Horányi, A., Muñoz-Sabater, J., et al. (2020). The ERA5 global reanalysis. *Quarterly Journal of the Royal Meteorological Society*, 146(730), 1999–2049. <https://doi.org/10.1002/qj.3803>
- Holland, J. Z., & Rasmusson, E. M. (1973). Measurements of the atmospheric mass, energy, and momentum budgets over a 500-Kilometer square of tropical ocean. *Monthly Weather Review*, 101(1), 44–55. [https://doi.org/10.1175/1520-0493\(1973\)101<0044:MAMEMB>2.3.CO;2](https://doi.org/10.1175/1520-0493(1973)101<0044:MAMEMB>2.3.CO;2)
- Janssens, M., de Arellano, J. V.-G., Scheffer, M., Antonissen, C., Siebesma, A. P., & Glassmeier, F. (2021). Cloud patterns in the trades have four interpretable dimensions. *Geophysical Research Letters*, 48(5), e2020GL091001. <https://doi.org/10.1029/2020GL091001>
- Klingebiel, M., Ghate, V. P., Naumann, A. K., Ditas, F., Pöhlker, M. L., Pöhlker, C., et al. (2019). Remote sensing of sea salt aerosol below trade wind clouds. *Journal of the Atmospheric Sciences*, 76(5), 1189–1202. <https://doi.org/10.1175/JAS-D-18-0139.1>
- Lamer, K., Kollias, P., & Nuijens, L. (2015). Observations of the variability of shallow trade wind cumulus cloudiness and mass flux. *Journal of Geophysical Research: Atmospheres*, 120(12), 2014JD022950. <https://doi.org/10.1002/2014JD022950>
- Löhner, U., & Crewell, S. (2003). Accuracy of cloud liquid water path from ground-based microwave radiometry 1. Dependency on cloud model statistics. *Radio Science*, 38(3), 8041. <https://doi.org/10.1029/2002RS002654>
- Lonitz, K., Stevens, B., Nuijens, L., Sant, V., Hirsch, L., & Seifert, A. (2015). The signature of aerosols and meteorology in long-term cloud radar observations of trade wind cumuli. *Journal of the Atmospheric Sciences*, 72(12), 4643–4659. <https://doi.org/10.1175/JAS-D-14-0348.1>
- Medeiros, B., & Nuijens, L. (2016). Clouds at Barbados are representative of clouds across the trade wind regions in observations and climate models. *Proceedings of the National Academy of Sciences*, 113(22), E3062–E3070. <https://doi.org/10.1073/pnas.1521494113>
- Nuijens, L., Serikov, I., Hirsch, L., Lonitz, K., & Stevens, B. (2014). The distribution and variability of low-level cloud in the North Atlantic trades. *Quarterly Journal of the Royal Meteorological Society*, 140(684), 2364–2374. <https://doi.org/10.1002/qj.2307>
- Nuijens, L., Stevens, B., & Siebesma, A. P. (2009). The environment of precipitating shallow cumulus convection. *Journal of the Atmospheric Sciences*, 66(7), 1962–1979. <https://doi.org/10.1175/2008JAS2841.1>
- Peters, G., Fischer, B., & Andersson, T. (2002). Rain observations with a vertically looking micro rain radar (MRR). *Boreal Environment Research*.
- Rasp, S., Schulz, H., Bony, S., & Stevens, B. (2020). Combining crowd-sourcing and deep learning to explore the meso-scale organization of shallow convection. *Bulletin of the American Meteorological Society*, 101, E1980–E1995. <https://doi.org/10.1175/BAMS-D-19-0324.1>
- Raspaud, M., Hoesse, D., Lahtinen, P., Dybbroe, A., Finkensieper, S., Roberts, W., & Valentino, A. (2019). Pytroll/satpy Version 0.16.0. Zenodo. <https://doi.org/10.5281/zenodo.3250583>
- Rauber, R. M., Ochs, H. T., Di Girolamo, L., Göke, S., Snodgrass, E., Stevens, B., et al. (2007). Rain in shallow cumulus over the ocean: The RICO campaign. *Bulletin of the American Meteorological Society*, 88(12), 1912–1928. <https://doi.org/10.1175/BAMS-88-12-1912>
- Riehl, H. (1945). *Waves in the easterlies and the polar front in the tropics: A report on research conducted at the institute of tropical meteorology of the university of Chicago at the university of Puerto Rico, Rio Piedras, P.R.* University of Chicago Press.
- Riehl, H. (1954). *Tropical meteorology*. McGraw-Hill.
- Satoh, M., Stevens, B., Judt, F., Khairoutdinov, M., Lin, S.-J., Putman, W. M., & Düben, P. (2019). Global cloud-resolving models. *Current Climate Change Reports*, 5(3), 172–184. <https://doi.org/10.1007/s40641-019-00131-0>
- Seidel, D. J., Fu, Q., Randel, W. J., & Reichler, T. J. (2008). Widening of the tropical belt in a changing climate. *Nature Geoscience*, 1(1), 21–24. <https://doi.org/10.1038/ngeo.2007.38>
- Seifert, A., & Heus, T. (2013). Large-eddy simulation of organized precipitating trade wind cumulus clouds. *Atmospheric Chemistry and Physics*, 13(11), 5631–5645. <https://doi.org/10.5194/acp-13-5631-2013>
- Seifert, A., Heus, T., Pincus, R., & Stevens, B. (2015). Large-eddy simulation of the transient and near-equilibrium behavior of precipitating shallow convection. *Journal of Advances in Modeling Earth Systems*, 7(4), 1918–1937. <https://doi.org/10.1002/2015MS000489>
- Siebesma, A. P., Bretherton, C. S., Brown, A., Chlond, A., Cuxart, J., Duynkerke, P. G., & Stevens, D. E. (2003). A large eddy simulation intercomparison study of shallow cumulus convection. *Journal of the Atmospheric Sciences*, 60, 19. [https://doi.org/10.1175/1520-0469\(2003\)60<019:alesis>2.0.co;2](https://doi.org/10.1175/1520-0469(2003)60<019:alesis>2.0.co;2)

- Siebesma, A. P., & Cuijpers, J. W. M. (1995). Evaluation of parametric assumptions for shallow cumulus convection. *Journal of the Atmospheric Sciences*, 52(6), 650–666. [https://doi.org/10.1175/1520-0469\(1995\)052<0650:EOPAFS>2.0.CO;2](https://doi.org/10.1175/1520-0469(1995)052<0650:EOPAFS>2.0.CO;2)
- Steinke, S., Eikenberg, S., Löhnert, U., Dick, G., Klocke, D., Di Girolamo, P., & Crewell, S. (2015). Assessment of small-scale integrated water vapour variability during HOPE. *Atmospheric Chemistry and Physics*, 15(5), 2675–2692. <https://doi.org/10.5194/acp-15-2675-2015>
- Stephan, C., Schnitt, S., Bellenger, H., Schulz, H., Szoéke, S. P. D., Acquistapace, C., & Stevens, B. (2020). Radiosonde measurements from the EUREC4A field campaign. AERIS. <https://doi.org/10.25326/62>
- Stevens, B., Ackerman, A. S., Albrecht, B. A., Brown, A. R., Chlond, A., Cuxart, J., et al. (2001). Simulations of trade wind cumuli under a strong inversion. *Journal of the Atmospheric Sciences*, 58(14), 1870–1891. [https://doi.org/10.1175/1520-0469\(2001\)058<1870:SOTWCU>2.0.CO;2](https://doi.org/10.1175/1520-0469(2001)058<1870:SOTWCU>2.0.CO;2)
- Stevens, B., Bony, S., Brogniez, H., Hentgen, L., Hohenegger, C., Kiemle, C., et al. (2020). Sugar, Gravel, Fish and Flowers: Mesoscale cloud patterns in the trade winds. *Quarterly Journal of the Royal Meteorological Society*, 146(726), 141–152. <https://doi.org/10.1002/qj.3662>
- Stevens, B., Farrell, D., Hirsch, L., Jansen, F., Nuijens, L., Serikov, I., et al. (2016). The barbados cloud observatory: Anchoring investigations of clouds and circulation on the edge of the ITCZ. *Bulletin of the American Meteorological Society*, 97(5), 787–801. <https://doi.org/10.1175/BAMS-D-14-00247.1>
- Ulbrich, U., Pinto, J. G., Kupfer, H., Leckebusch, G. C., Spangehl, T., & Reyers, M. (2008). Changing northern hemisphere storm tracks in an ensemble of IPCC climate change simulations. *Journal of Climate*, 21(8), 1669–1679. <https://doi.org/10.1175/2007JCLI1992.1>
- Vial, J., Vogel, R., & Schulz, H. (2021). On the daily cycle of mesoscale cloud organization in the winter trades. *Quarterly Journal of the Royal Meteorological Society*. <https://doi.org/10.1002/qj.4103>
- Yin, J. H. (2005). A consistent poleward shift of the storm tracks in simulations of 21st century climate. *Geophysical Research Letters*, 32(18), L18701. <https://doi.org/10.1029/2005GL023684>
- Zuidema, P., Li, Z., Hill, R. J., Bariteau, L., Rilling, B., Fairall, C., et al. (2012). On trade wind cumulus cold pools. *Journal of the Atmospheric Sciences*, 69(1), 258–280. <https://doi.org/10.1175/JAS-D-11-0143.1>